Observed Synergies between Urban Heat Islands and Heat Waves and Their Controlling Factors in Shanghai, China

XIANGYU AO

Shanghai Meteorological Service, and Shanghai Key Laboratory of Meteorology and Health, Shanghai, China

LIANG WANG

Department of Earth and Environment, Boston University, Boston, Massachusetts

XING ZHI, WEN GU, AND HEQUN YANG

Shanghai Meteorological Service, Shanghai, China

DAN LI

Department of Earth and Environment, Boston University, Boston, Massachusetts

ABSTRACT

There is an ongoing debate as to whether the UHI intensity (UHII) is enhanced or dampened under heat waves (HWs). Using a comprehensive dataset including continuous surface energy flux data for three summers (2016–18) and automated weather station data for six summers (2013–18) in Shanghai, China, we find synergies between UHIs and HWs when either a coastal or an inland suburban site is used as the reference site. We further find that during HWs, the increase of net radiation at the urban site is larger than that at the suburban site. More importantly, the latent heat flux is slightly reduced at the urban site but is slightly increased at the suburban site, while the increase of the sensible heat flux is larger at the urban site. This change of surface energy partitioning, together with the increased anthropogenic heat flux during HWs, exacerbates the UHII. The change of surface energy partitioning is consistent with the observed decrease of relative humidity ratio between urban and suburban areas. The UHII is stronger when the regional wind speed is reduced and under sea breeze, both of which are found to be associated with HWs in our study region. This study suggests that there are multiple factors controlling the interactions between UHIs and HWs, which may explain why synergies between UHIs and HWs are only found in certain metropolitan regions and/or under certain HW events.

1. Introduction

Heat waves (HWs) have received much attention from scientists and policy makers because of their adverse effects on human health (Kalkstein et al. 2008). For example, the 2003 European HW (Zaitchik et al. 2006), the 2010 Russian HW (Grumm 2011), the 2012 U.S. HW (Knutson et al. 2013), and the record-breaking HW event in eastern China in 2013 (Xia et al. 2016; Ma et al. 2017) all caused numerous deaths. HWs also have severe impacts on air quality, energy consumption, crop production, and ecosystem services (Hoffert et al. 2002;

Miller et al. 2008; Wreford and Neiladger 2010; Depietri et al. 2012; Geddes et al. 2014; Cao et al. 2015). An HW generally refers to an extremely hot period that can last for several days or weeks (Robinson 2001) and is typically instigated by a synoptic-scale high pressure system (Matsumura et al. 2015), which severely restrains the formation of convective clouds (He et al. 2015). As a result, the weather during an HW is usually characterized by light wind and cloudless sky. In a warming climate, the frequency, intensity, duration, and spatial extent of HWs are expected to be exacerbated (Meehl and Tebaldi 2004; Li et al. 2012; Lau and Nath 2012; Loikith and Broccoli 2012; Lau and Ploshay 2013; Peterson et al. 2013; Russo et al. 2015; Mora et al. 2017).

Corresponding author: Dan Li, lidan@bu.edu

Urban residents are arguably more vulnerable to HWs than those in suburban or rural areas because of the urban heat island (UHI) effect; that is, cities are usually hotter than the surrounding suburban or rural areas, although larger mortality rates might occur in rural areas under HWs because of the limited access to air conditioning and/or medical facilities (Hu et al. 2019). The UHI effect is one of the most notable and studied climatic impacts of cities (Oke 1982; Grimmond 2007). The primary reason for the formation of an UHI is the replacement of natural surface by urban land characterized by increased roughness, limited green spaces, lower albedo, and higher heat capacity, as well as significant anthropogenic heat emissions (Oke 1982). These alterations lead to modifications of the urban surface energy and water balances and create the unique urban climate features such as the UHI (Roth 2000; Arnfield 2003; Kalnay and Cai 2003; Zhou et al. 2004; Miao et al. 2009). Meanwhile, meteorological conditions (e.g., cloud cover and wind field) and geographical locations (e.g., inland or coastal) also have substantial impacts on the UHI intensity (UHII; Zhao et al. 2014; Zhou et al. 2015). Since cloud cover and wind speed can change significantly under HWs, it is very likely that HWs may have an influence on the UHII (Basara et al. 2010). However, studies on how UHIs are modulated by HWs are still limited, despite its significance for a variety of important issues including human health (Anderson and Bell 2009; Tan et al. 2010; Anderson and Bell 2011; Gabriel and Endlicher 2011).

A number of recent studies examined the alteration of UHII by HWs in the city of Baltimore, Maryland (Li and Bou-Zeid 2013); the city of Beijing, China (Li et al. 2015, 2016); the city of Madison, Wisconsin, in the north-central United States (Schatz and Kucharik 2015); New York City, New York (Ramamurthy et al. 2017); and the coastal city of Athens, Greece (Founda et al. 2015; Founda and Santamouris 2017). All of these studies discovered synergistic interactions between UHIs and HWs; namely, the UHII was enhanced under HWs. They indicated that such synergies are primarily attributed to the contrasting responses of urban and rural surface energy budgets to HWs (see, e.g., Li et al. 2015) and changes in the ambient wind speed (see, e.g., Li et al. 2016). Sun et al. (2017) also emphasized the role of heat storage, which often experiences a significant increase during daytime under HWs and is later released during nighttime. However, other factors such as the anthropogenic heat flux have received less attention. In addition, how HWs affect the UHI intensity through altering wind patterns including urban-breeze circulation (Haeger-Eugensson and Holmer 1999; Hidalgo et al. 2010) and land-breeze–sea-breeze circulation

(Founda and Santamouris 2017), the latter of which is particularly important for coastal cities, is also understudied.

While many studies reported synergistic interactions between UHIs and HWs, a number of studies also found insignificant or nonexistent synergistic effects. For example, Zhou and Shepherd (2010) found that whether the synergistic effect in Atlanta is significant or not depends on which station is chosen as the rural reference. Ramamurthy and Bou-Zeid (2017) conducted a comparative analysis of multiple cities over the northeastern United States and found synergistic effects in New York City; Washington, D.C.; and Baltimore but not in Philadelphia, Pennsylvania. A recent modeling study by Zhao et al. (2018) found significant spatial and temporal variabilities in the interactions between UHIs and HWs across 50 U.S. cities: clear daytime synergistic effects are discovered in temperate regions while insignificant effects are found in dry regions in the current climate. However, in the future climate the synergistic effects in temperate regions diminish, but significant effects start to emerge in dry regions. In another recent observational study, Scott et al. (2018) found that the UHII tends to decrease with increasing temperature in most U.S. cities (38 of 54), which also holds true for heat extremes.

The ongoing debate about whether there are synergies between UHIs and HWs, together with the previously mentioned need to better understand the roles of anthropogenic heat flux and the wind pattern (including land-breeze–sea-breeze circulation) in the context of UHI–HW synergies, motivates us to revisit the interactions between UHIs and HWs using a comprehensive dataset including continuous surface energy flux data for three summers (2016–18) and automated weather station data for six summers (2013–18) collected in the city of Shanghai, China, which is the most populous megacity in China located on the east coast and in the subtropical monsoon climate zone (Cui and Shi 2012). This has important local implications as extreme HWs in Shanghai have shown an increasing trend in recent years (Xia et al. 2016; Ma et al. 2017). The objectives of this study are twofold: 1) to quantify the UHII under HW and non-HW (NHW) conditions using observational data, and 2) to investigate the responses of urban and suburban surface energy budgets, including the anthropogenic heat flux, and the ambient meteorological conditions such as the wind field, to HWs.

2. Data and methods

a. Data

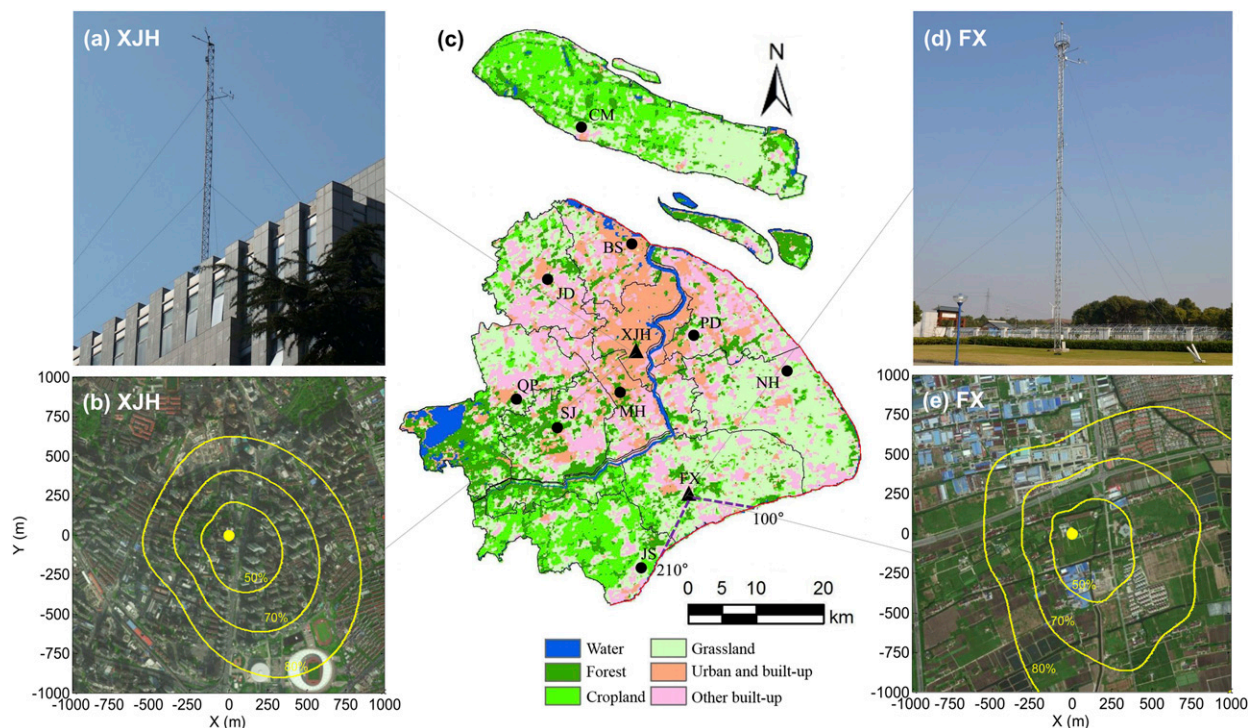The data used in this study include radiation and turbulent fluxes measured at two sites (see Fig. 1), an

FIG. 1. Flux towers at the (a) urban (XJH) and (d) suburban (FX) sites, and the land-cover characteristics within 1 km² around (b) XJH and (e) FX overlaid by the cumulative flux source areas (footprint). The contours represent the percentage of the source area. (c) Land-use map of Shanghai derived from MODIS 250-m (2015) data and the locations of 11 automated weather stations. The urban (XJH) and suburban (FX) sites have simultaneous flux observations. The coastline is shown as the red boundary. The gray dotted lines denote the approximate sea-breeze regimes for the FX site.

urban site [Xujiahui (XJH)] and a suburban site [Fengxian (FX)], in Shanghai for three summer seasons (July–August) from 2016 to 2018. The urban site (31.19°N, 121.43°E) is located in a business district with the 25-m-high flux tower installed on the rooftop of a 55-m-high building; hence the sensor height is 80 m above ground level (agl) [see Fig. 1a and further details in Ao et al. (2016a)]. Buildings around the urban site are tall and dense. The suburban site (30.89°N, 121.5°E) has a 28-m-high flux tower directly installed on the ground (Fig. 1d). Buildings around the suburban site are sparse and small. The two sites use the same instruments. Incoming and outgoing shortwave and longwave radiation fluxes are measured by a net radiometer (Kipp and Zonen model CNR4) sampled every 1 min, and half-hourly averages are used for analysis. Turbulence measurements are collected with the Campbell Scientific, Inc., ''IRGASON'' model open-path gas analyzer integrated with a three-dimensional sonic anemometer mounted to the prevailing southeast wind direction. Turbulence signals are sampled at 10 Hz with a CR3000 datalogger. The raw turbulence data are carefully quality controlled and fluxes are computed using the eddy-covariance method at 30-min intervals. Detailed quality

control measures and flux calculations can be found in Ao et al. (2016a,b).

Hourly meteorological data including 2-m (agl) air temperature T_{2m}, 10-m (agl) wind speed and direction, relative humidity, and precipitation for six years (2013–18) are also measured by 11 automated weather stations (AWSs). Each of the two flux towers has a collocated AWS. These AWS data are used for HW identification, UHII calculation, and other analysis. In particular, the 10-m wind speed data averaged over all 11 AWSs are used to represent the regional wind speed in Shanghai.

b. Methods

1) SOURCE AREAS OF TURBULENT FLUXES

To better understand the measured turbulent fluxes, the cumulative turbulent flux source areas (or footprints) for the study period at the two sites are estimated using an analytical two-dimensional footprint model (Kormann and Meixner 2001; Christen et al. 2011). Source areas for every 30-min period are modeled and then aggregated for the whole study period. Model inputs include the measurement height, roughness length, wind speed and direction, crosswind speed standard

deviation, friction velocity, and the Obukhov length. Figures 1b and 1e show the integrated source areas as contours overlaid above land-cover aerial photographs around the two sites. It can be seen the overall shapes of the source areas for both sites are toward the southeast, which is the prevailing wind direction. The sizes of the footprint area are similar at the two sites. The 80% footprint area at the urban site extends about 850 m to the southeast and 500 m to the northwest. The 80% footprint area for the suburban site is a bit larger, exceeding 1 km to the southeast and also extending to about 500 m to the northwest. The total contribution percentages for a 1-km^2 area are 94% and 88% for the urban and suburban sites, respectively. As such, these 1-km^2 areas can roughly represent the main source areas. Based on GIS data provided by Shanghai Surveying and Mapping Institute (http://www.shsmi.cn/) and a field survey of surface metadata, the mean building height and surface cover information are derived within the 1-km^2 areas of the two sites (Table 1). It is clear that the mean building height around the urban site is much larger. The surface cover at the urban site is dominated by buildings and roads, while grasses and trees are the dominant vegetation types at the suburban site.

2) DEFINITIONS OF UHII AND HW

Different studies often define the UHII using different temperature metrics and in different ways. For example, previous studies have used the urban–uburban/rural difference of daily mean or hourly air temperature, daily maximum air temperature, surface skin temperature and so on to define the UHII (Tan et al. 2010; Y. Liu et al. 2018). Because the 2-m air temperature T_{2m} can directly affect human thermal comfort, we define the UHII as the difference in T_{2m} between the urban (XJH) site and the reference site. The temperature for the reference site could be from a single site or averaged over several suburban/rural sites. Here we use two reference sites to compute the UHII at hourly scales. We first use the FX site as our reference site because it has radiation and flux measurements (see Fig. 1) and has the second largest vegetation cover fraction (0.63) among the 11 AWSs in Shanghai with a relatively long distance (34 km) from the XJH urban site. However, since the FX site is only about 8 km from the sea and hence might be influenced by the land-breeze–sea-breeze circulation, an inland (50 km from the sea) suburban site [Qingpu (QP)] (31.13°N, 121.12°E) located 30 km to the west of the urban site is also chosen as a reference site for comparison. The QP site has the largest vegetation cover fraction (0.64) among the 11 AWSs. The other 8 AWSs are located at places with relatively high impervious surface cover fractions so that they are not suitable

TABLE 1. Average building heights and land-cover fractions within 1 km^2 around the urban (XJH) site and the suburban (FX) site.

Site	Z_H (m)	Paved	Building	Trees	Grass	Bare soil	Water
Urban	36	0.62	0.23	0.04	0.1	0	0.01
Suburban	6	0.2	0.14	0.1	0.53	0.02	0.01

for being used as reference sites (D. Liu et al. 2018). It should be stressed that the hourly UHII is calculated using 2-m air temperature measurements from the AWSs (hence 2 m refers to 2 m agl), not measurements from the flux towers (i.e., 2 m does not mean 2 m above the rooftop).

The HW definition also remains an open question, and existing definitions from the literature vary with respect to the threshold value for temperature extremes, duration of hot days, etc. Here a HW is defined as a period that has at least three consecutive days with daily maximum $T_{2m} \geq 35°C$ (hot day) at the urban (XJH) site. This definition is consistent with the high temperature alert from Chinese Meteorological Administration. Because there are no HW days in June, the study period is chosen to be July–August. The remaining days are termed NHW days. According to this definition, 12 HW events (100 HW days and 272 NHW days) during 2013–18, and 6 HW events (52 HW days and 134 NHW days) during 2016–18 have been selected. The large-scale weather pattern responsible for HW events in East Asia is mainly the western North Pacific subtropical high (WNPSH) (Enomoto 2004; Kim and Lee 2006; He et al. 2015). The contour of 588 dagpm at 500-hPa level is widely used as a benchmark to represent the location of WNPSH (He et al. 2015). Figure 2 shows the mean geopotential height at 500-hPa level based on the National Centers for Environmental Prediction (NCEP) Final (FNL) dataset at 0800 LST under NHW and HW conditions during 2013–18. The geopotential height at 500 hPa under NHW conditions is much lower than that under HW conditions, and Shanghai is located to the west edge of the 576-dagpm contour. In contrast, under HW conditions, the WNPSH controls a large part of eastern China, including Shanghai, which is located near the center of the WNPSH.

Since the UHII is strongly influenced by cloud cover and type, wind speed, humidity and precipitation, we further classify the HW and NHW days into "optimal" and "nonoptimal" categories following Eastin et al. (2018). When the sky is clear, the daily mean regional wind speed (defined as the average wind speed of the 11 AWSs) is less than 2.5 m s^{-1}, the daily mean relative humidity is less than 80% and there is no precipitation, the day is defined as optimal because the UHII is
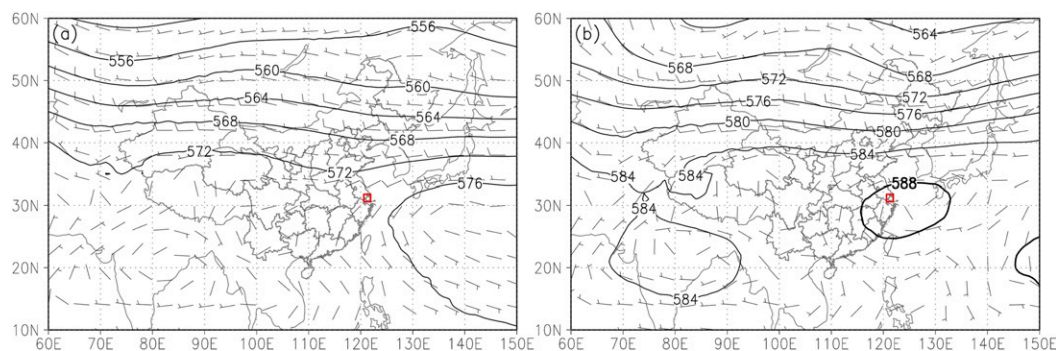
FIG. 2. The mean geopotential height (dagpm; contours) and wind field at 500 hPa under (a) NHW and (b) HW conditions during 2013–18. The red rectangle denotes the location of Shanghai. The solid 588-dagpm line in (b) represents the location of the WNPSH.

expected to be the strongest under such conditions. Otherwise the day is defined as nonoptimal for identifying the UHI effect. To determine the sky conditions, we use the daily mean bulk atmospheric transmissivity τ calculated from the daily total incoming shortwave radiation and the solar radiation at the top of the atmosphere (Ao et al. 2016b). When $\tau \geq 0.7$, it is classified as a clear day.

This classification yields a total of 35, 65, 16, and 256 days for HW optimal, HW nonoptimal, NHW optimal, and NHW nonoptimal categories, respectively, during 2013–18 and 16, 36, 11, and 123 days during 2016–18. The basic meteorological variables under these four categories (HW optimal, HW nonoptimal, NHW optimal, and NHW nonoptimal) for daily, daytime ($K\downarrow > 0\,\mathrm{W\,m^{-2}}$), and nighttime ($K\downarrow = 0\,\mathrm{W\,m^{-2}}$) mean over 2013–18 are summarized in Table 2. One can see that the daytime mean atmospheric transmissivity τ is equal to 0.7 under both HW and NHW conditions for the optimal category (as expected), whereas τ is larger under HW than NHW conditions for the nonoptimal category, suggesting overall less cloud cover under HW conditions. The daytime mean incoming shortwave radiation at the urban site has similar magnitude between HW and NHW conditions (487.1 and 486.0 W m^{-2}, respectively) for the optimal category, while much larger during HW than NHW conditions (408.1 and 300.5 W m^{-2}, respectively) for the nonoptimal category. This implies that overall the incoming shortwave radiation is stronger under HW conditions. For the nonoptimal category only in which precipitation occurs, the daily total precipitation is the largest at the urban site, second largest at the coastal FX site, followed by the inland QP site. The surface pressure is similar among sites and categories and shows small changes between HW and NHW conditions. Other meteorological conditions are discussed later when the synergies between UHIs and HWs are examined.

3) THE SURFACE ENERGY BALANCE

The surface energy balance equation is often written as

$$Q^* + Q_F = Q_H + Q_E + \Delta Q_S, \tag{1}$$

where Q^* is the net all-wave radiation ($Q^* = K\downarrow - K\uparrow + L\downarrow - L\uparrow$). The four components of Q^* are incoming ($\downarrow$) and outgoing ($\uparrow$) shortwave (K) and longwave (L) radiation. Term Q_F is the anthropogenic heat flux. The urban Q_F is usually larger than that in suburban areas, but accurate estimation of Q_F remains challenging [more details can be found in section 2b(5)]. Term Q_H is the sensible heat flux, which is the main source for heating the atmosphere (when $Q_H > 0$). Term Q_E is the latent heat flux from evapotranspiration of vegetation and soil. The ΔQ_S is the heat flux stored into the surface and the building volume, including various facets (ground, walls, roofs, etc.), which is difficult to measure directly and is usually estimated as the residual of the surface energy balance. Because this residual method aggregates the errors in all other terms, including the well-known surface energy balance closure problem [see Foken (2008) for a review] and the horizontal heat advection due to the large thermal contrast between land and sea for coastal sites, into ΔQ_S, ΔQ_S is not specifically analyzed in this study.

4) AN ANALYTICAL MODEL FOR UHII

An analytical model developed by Li and Bou-Zeid (2013) is employed here to facilitate our understanding of the physical mechanisms behind the interactions between UHIs and HWs. The model is based on the simplified two-dimensional heat and water vapor advection–diffusion equations coupled with the surface energy balance equation, and simultaneously solves the vertical turbulent transport and horizontal advection of heat and water vapor exchanges between a limited

TABLE 2. Daily, daytime, and nocturnal mean meteorological variables at three sites (urban: XJH; suburban: FX and QP) for different weather conditions. OPT and NOPT denote optimal and nonoptimal dates, respectively, and ALL denotes the two combined.

Variable		Daily						Day						Night					
		HW OPT	HW NOPT	HW ALL	NHW OPT	NHW NOPT	NHW ALL	HW OPT	HW NOPT	HW ALL	NHW OPT	NHW NOPT	NHW ALL	HW OPT	HW NOPT	HW ALL	NHW OPT	NHW NOPT	NHW ALL
T_{2m} (°C)	XJH	32.7	32.3	32.4	29.6	28.3	28.4	34.5	33.8	34.0	31.0	29.3	29.4	30.6	30.4	30.5	27.9	27.2	27.2
	FX	31.0	31.0	31.0	28.2	27.7	27.7	32.6	32.7	32.6	29.7	28.7	28.8	29.0	29.0	29.0	26.3	26.4	26.4
	QP	32.0	31.6	31.8	28.7	27.9	28.0	34.1	33.7	33.8	30.7	29.3	29.4	29.4	29.1	29.2	26.3	26.4	26.4
UHII (°C)	FX	1.76	1.23	1.42	1.43	0.66	0.70	1.87	1.11	1.38	1.27	0.57	0.61	1.63	1.39	1.47	1.63	0.76	0.81
	QP	0.72	0.65	0.68	0.91	0.39	0.43	0.34	0.10	0.19	0.28	0.04	0.06	1.20	1.32	1.28	1.65	0.80	0.85
RH (%)	XJH	61.6	63.2	62.6	65.7	77.0	76.4	54.6	56.9	56.1	59.2	72.6	71.8	70.2	70.9	70.6	73.4	82.3	81.8
	FX	75.1	75.4	75.3	76.1	84.0	83.6	68.2	68.3	68.2	68.4	79.1	78.5	83.6	84.2	84.0	85.2	89.8	89.6
	QP	67.6	69.5	68.8	71.7	80.4	79.9	58.3	60.4	59.6	62.8	74.4	73.7	79.0	80.7	80.1	82.2	87.4	87.1
Wind speed ($m\,s^{-1}$)	XJH	0.6	0.7	0.7	0.6	0.7	0.7	0.8	0.9	0.9	0.8	0.8	0.8	0.5	0.5	0.5	0.4	0.5	0.5
	FX	2.7	2.7	2.7	2.7	3.1	3.0	3.0	3.0	3.0	3.4	3.5	3.5	2.3	2.2	2.2	1.9	2.5	2.5
	QP	2.0	2.0	2.0	2.3	2.5	2.5	2.3	2.3	2.3	2.7	2.9	2.9	1.7	1.6	1.6	1.8	2.1	2.1
	Regional	2.0	2.1	2.0	2.1	2.3	2.3	2.3	2.4	2.3	2.6	2.7	2.7	1.7	1.7	1.7	1.6	2.0	1.9
Pressure (hPa)	XJH	1005.3	1005.3	1005.3	1006.1	1005.2	1005.2	1005.2	1005.3	1005.2	1005.9	1005.0	1005.1	1005.4	1005.4	1005.4	1006.3	1005.3	1005.3
	FX	1005.5	1005.5	1005.5	1006.2	1005.2	1005.2	1005.5	1005.5	1005.5	1006.1	1005.1	1005.1	1005.5	1005.5	1005.5	1006.3	1005.2	1005.3
	QP	1005.3	1005.3	1005.3	1006.1	1005.2	1005.2	1005.3	1005.3	1005.3	1006.0	1005.1	1005.1	1005.4	1005.4	1005.4	1006.3	1005.3	1005.4
Rain (mm)	XJH	0.0	30.9	30.9	0.0	290.8	290.8	0.0	21.9	21.9	0.0	177.0	177.0	0.0	8.6	8.6	0.0	113.7	113.7
	FX	0.0	4.0	4.0	0.0	273.8	273.8	0.0	3.7	3.7	0.0	159.2	159.2	0.0	0.3	0.3	0.0	114.2	114.2
	QP	0.0	32.3	32.3	0.0	257.2	257.3	0.0	20.0	20.0	0.0	137.4	137.4	0.0	11.2	11.2	0.0	119.7	119.8
τ								0.7	0.6	0.6	0.7	0.4	0.4	0.0	0.0	0.0	0.0	0.0	0.0
$K\downarrow$ (W m^{-2})								487.1	408.1	435.7	486.0	300.5	311.5	0.0	0.0	0.0	0.0	0.0	0.0

urban surface and the atmosphere. It assumes a given regional wind speed profile and the upwind cooler rural air is advected to the downwind urban area, which has a contrasting surface energy budget because of different thermodynamic surface properties. The advected air is hence heated over the urban area by the larger sensible heat flux and forms an urban thermal boundary layer. Full details about the derivation and development of this model can be found in Li and Bou-Zeid (2013). A summary of the model, including the final expression for the UHII, is presented for reference in the appendix.

5) ESTIMATION OF ANTHROPOGENIC HEAT FLUX

The estimation of Q_F remains difficult and challenging given its dependence on many factors and the lack of detailed city-specific energy consumption data (Sailor 2011; Chow et al. 2014; Sailor et al. 2015). Here the Large Scale Urban Consumption of Energy (LUCY) QF model (hereinafter the LQF model) (Allen et al. 2011; Lindberg et al. 2013; Gabey et al. 2018) is employed to estimate the hourly Q_F during the study period. The LQF model takes a top-down approach based on annual energy consumption data for a relatively large area (e.g., a country or a city) and distributes the heat emissions across the area of interest according to high-resolution population data. The LQF model divides Q_F into three subcomponents: building, transport, and metabolism. The daily totals vary with the daily temperature and the diurnal patterns are based on prescribed diurnal profiles that differ between weekdays and weekends. The daily building energy consumption is related to the daily air temperature via a temperature response function including several city-specific parameters. The original temperature response function (Lindberg et al. 2013) is modified by replacing the only one threshold temperature with two threshold temperatures to determine cooling or heating. Another five parameters include two threshold temperatures where saturation energy use occurs (cooling and heating) and three nondimensional coefficients related to the comfortable temperature range, cooling and heating rates. These parameters are determined for Shanghai using annual total energy consumption data obtained from the Shanghai statistical year book and five years (2005–09) of city-level hourly electricity consumption data (Liu and Cao 2013). The hourly electricity consumption data are combined with the daytime/nighttime population density (Yu and Wen 2016; Zhong et al. 2017) to derive the diurnal profiles of anthropogenic heat flux from buildings. The diurnal profiles of anthropogenic heat flux from traffic are based on hourly highway traffic count data of the inner ring of Shanghai in 2011. The diurnal pattern of anthropogenic heat flux from metabolic emission

follows Sailor and Lu (2004) with a minimum of 75 W, a maximum of 175 W, and a transition value of 125 W per capita. The model results indicate that the building emissions are the dominant component. More details about the implementation and application of the LQF model in the Shanghai region can be found in Ao et al. (2018).

We acknowledge that the input data for the LQF model do not match the study period. However, we find that the mean diurnal profiles of electricity consumption for each year from 2005 to 2009 are quite similar to each other, which gives us confidence to assume that the diurnal profile for the study period is the same as that in 2005–09. The mean diurnal profiles for the traffic data in the four seasons of 2011 are also similar so we use the mean diurnal profile of 2011 as the proxy for the study period.

3. Results

a. Observed synergies between UHIs and HWs

Before we examine the synergies between UHIs and HWs, it is important to understand the differences in the UHII calculated based on two different reference sites (Table 2). The order of T_{2m} from high to low are the urban XJH site, the inland QP site, and the coastal FX site under every category, indicating persistent UHI and coastal cooling effects. The daily and daytime mean UHII for the coastal FX site is significantly stronger than those for the inland QP site, with values 0.7°–1.8°C versus 0.4°–0.9°C and 0.6°–1.9°C versus 0.0–0.3°C, respectively. On the other hand, the nocturnal UHII for the FX and QP sites are close to each other with values 0.8°–1.6°C versus 0.8°–1.2°C. This is likely due to the fact that land breeze prevails during night and hence both FX and QP sites experience the same advective conditions. The UHII for the FX site under HW conditions is consistently larger than (or equal to) its NHW counterparts, indicating synergistic interactions between HWs and UHIs. The UHI for the QP site is larger during HWs for the "all" (optimal plus nonoptimal) and nonoptimal categories, as well as the daytime optimal category. The statistical significance of all UHII results in Table 2 have been assessed. All UHII results are significant at the 95% confidence level except under HW nonoptimal (UHII = 0.1°C) and NHW nonoptimal (UHII = 0.04°C) during daytime with the QP reference site.

Figure 3 shows the average diurnal variations of T_{2m} at the urban (XJH) and suburban (FX and QP) sites and the computed UHII under different conditions (all, HW optimal, NHW optimal, HW nonoptimal, and NHW nonoptimal) in the six summers (July–August) from 2013 to 2018. It can be seen that T_{2m} at both the urban and suburban sites are much higher under HW conditions
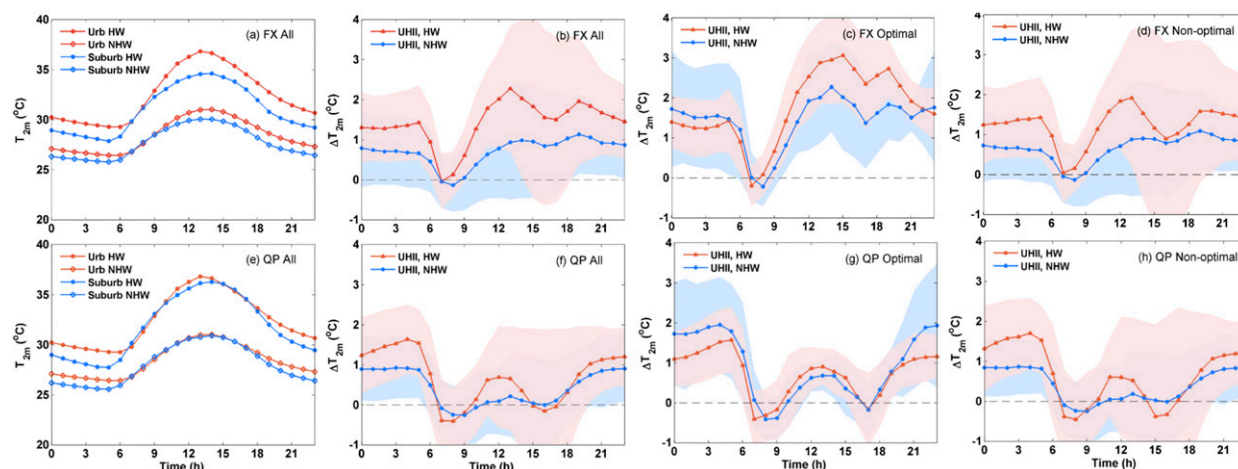
FIG. 3. Mean diurnal variations of 2-m air temperature at the urban (XJH) site and the suburban (a) FX and (e) QP sites, and comparing the UHII (between XJH and the suburban sites) under HW and NHW conditions for (b),(f) all categories, (c),(g) the optimal category, and (d),(h) the nonoptimal category. The shaded areas denote standard deviations.

than under NHW conditions. When the coastal (FX) site is used as the reference site and all meteorological conditions are considered, T_{2m} is considerably higher at the urban site throughout the day except in the early morning from 0700 to 0800 LST, exhibiting a clear UHI phenomenon. The UHII shows a clear increase during HW conditions, which indicates synergistic interactions between UHIs and HWs. The daily maximum UHII during HWs (2.3°C) occurs in the early afternoon (1300 LST), but its counterpart during NHWs (1.1°C) occurs in the late evening (1900 LST). The afternoon peak of UHII during HWs is consistent with a previous study in Shanghai (Tan et al. 2010) but is different from the case in Beijing (Li et al. 2015), where the UHII and the synergistic interactions between UHIs and HWs are the strongest at night. The daytime maximum of UHII when the coastal (FX) site is used as the reference site can be influenced by the local land-breeze–sea-breeze circulation and the steady daytime sea surface temperature. When divided into optimal and nonoptimal categories, the diurnal patterns of UHII remain similar but with much larger magnitude for the optimal category. The synergistic effects are clear for both optimal and nonoptimal categories.

The UHII computed using the inland (QP) site as the reference site is smaller than that computed using the coastal (FX) site as the reference site from 0700 to 2200 LST, which is consistent with the results in Table 2. The diurnal pattern of UHII for the QP site is very different from that for the FX site (Fig. 3), with daily maximum of 1.6° and 0.9°C for HW and NHW conditions, respectively, observed at night (around 0400 LST). The synergistic interactions between HWs and UHIs are also prominent for the QP site under nonoptimal

conditions. For the optimal category, the synergistic effects only exist during daytime (Fig. 3g). The fact that the synergies disappear for the optimal category at night may be due to cloud effects. Note that the definition of clear sky that is based on atmospheric transmissivity is only suitable for daytime conditions. However, overall the synergistic effects are observed at both daytime and nighttime when the QP site is used as the reference site.

b. The role of land–sea-breeze circulation

Previous studies show that wind direction has a substantial influence on the magnitude of UHII especially for coastal cities because of the existence of land-breeze–sea-breeze circulation (Chen et al. 2011; Meir et al. 2013; Founda and Santamouris 2017). The land breeze–sea breeze in this paper is defined at hourly scale rather than daily scale as the land-breeze–sea-breeze circulation has obvious diurnal variations. According to the coastline shape of Shanghai (Fig. 1), when the hourly wind direction measured at the coastal site (in this case the FX site) lies between 100 and 210° (southerly), it corresponds to sea breeze. When the hourly wind direction is in the ranges of 0°–90° or 270°–360° (northerly), it corresponds to land breeze. Figures 4a and 4b show the diurnal cycle of UHII using the coastal (FX) reference site for land-breeze (0°–90° or 270°–360°) and sea-breeze (100°–210°) cases under HW and NHW conditions during 2013–18. It can be seen synergistic interactions between HWs and UHIs exist both for land-breeze and sea-breeze cases. The fraction of data for HW land-breeze cases is only 2.4%, which results in more fluctuated diurnal curves. The daily maximum of UHII for land-breeze case occurs at night, which is similar to that
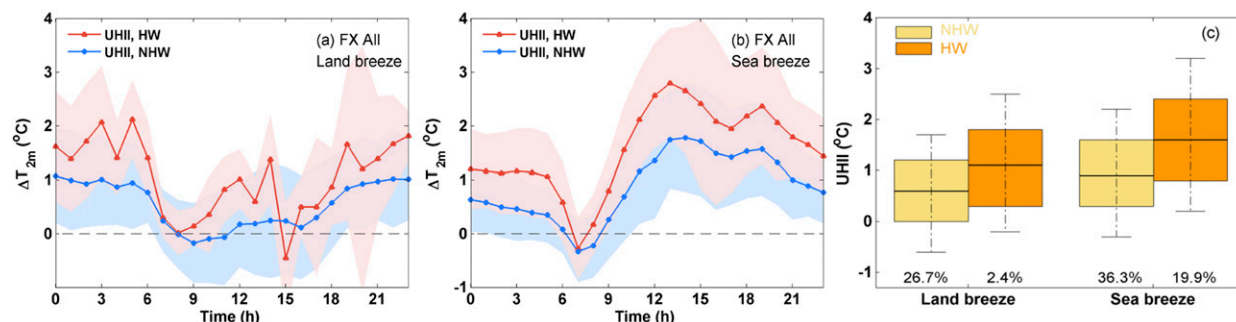
FIG. 4. The UHII based on the coastal (FX) site under HW and NHW conditions for all categories for (a) land-breeze and (b) sea-breeze cases; the shaded areas denote standard deviations. Also shown are (c) boxplots of UHII separated by land breeze and sea breeze under HW and NHW conditions; the percentages represent the data availability.

case based on the inland (QP) reference site, while the daily maximum of UHII for sea-breeze case occurs in the daytime. Figure 4c presents boxplots of the UHII grouped by land-breeze and sea-breeze cases under HW and NHW conditions during 2013–18. Interestingly, we find that sea breeze prevails under HW conditions (i.e., there are more data points associated with sea breeze than land breeze under HW conditions). According to Fig. 4c, the magnitude of UHII is intensified by sea breeze, and further intensified by HWs. The median values for UHII for land-breeze and sea-breeze cases under NHW conditions are 0.6° and 0.9°C, respectively, while the counterparts for land-breeze and sea-breeze cases under HW conditions are 1.1° and 1.6°C, respectively. This stronger UHII under sea breeze is because sea breeze acts as a cooling mechanism for the coastal site (in this case the suburban site). Our results are consistent with findings in Athens (Founda and Santamouris 2017).

c. Contrasting responses of the urban and suburban surface energy budgets to HWs

To understand the observed synergies between UHIs and HWs, the responses of the urban and suburban surface energy budgets to HWs are analyzed. We note that radiation and turbulent flux data are only available during 2016–18 and only for the XJH urban site and the FX suburban site, but we find that the synergies between HWs and UHIs averaged over 2016–18 are very similar to those over 2013–18 for both FX and QP sites (not shown). As such, the available radiation and turbulent flux data should provide important insights into the mechanisms responsible for the observed synergies.

We start with examining the shortwave radiation (Figs. 5a–d), the longwave radiation (Figs. 5e–h), and the net all-wave radiation (Figs. 6a,b). We then investigate the partition of available energy (the sum of sensible and latent heat fluxes) into sensible heat and

latent heat fluxes (Figs. 6c–f). The anthropogenic heat flux is further examined in Figs. 6g and 6h. In Figs. 5 and 6, we focus on the differences between HW and NHW conditions (represented by the symbol Δ). As a comparison, we further examine the urban–suburban differences (represented by the symbol δ) in Fig. 7.

1) DIURNAL VARIATIONS OF RADIATION BUDGETS

Figures 5a–d show the results of incoming and outgoing shortwave radiation ($K\downarrow$ and $K\uparrow$, respectively). It can be seen $K\downarrow$ at the urban and suburban sites are very close to each other under both HW and NHW conditions. The upward shortwave radiation flux at the urban site is smaller than its suburban counterpart, indicating a smaller urban albedo possibly due to the use of dark materials and radiative trapping by 3D building structures. Both $K\downarrow$ and $K\uparrow$ at urban and suburban sites show obvious increases, especially at noon during HW periods. This is consistent with the fact that HWs are generally associated with cloudless sky. The increase of $K\downarrow$ at the urban site is larger than that of the suburban site, while the increases of $K\uparrow$ at urban and suburban sites are similar, and hence there is more net shortwave radiation input during HWs at the urban sites than at the suburban site.

Figures 5e–h show the average diurnal variations of downward and upward longwave radiation ($L\downarrow$ and $L\uparrow$, respectively) under HW and NHW conditions. The $L\downarrow$ and $L\uparrow$ are amplified during HWs at both urban and suburban sites, and the increases at the urban site are stronger. The strongest increase occurs at 1300 LST, which is consistent with the occurrence of the daily maximum temperature. This is expected given the strong link between the longwave radiation and air temperature through the Stefan–Boltzmann law.

Integrating the four radiation components yields the net all-wave radiation flux Q^*, whose diurnal characteristics
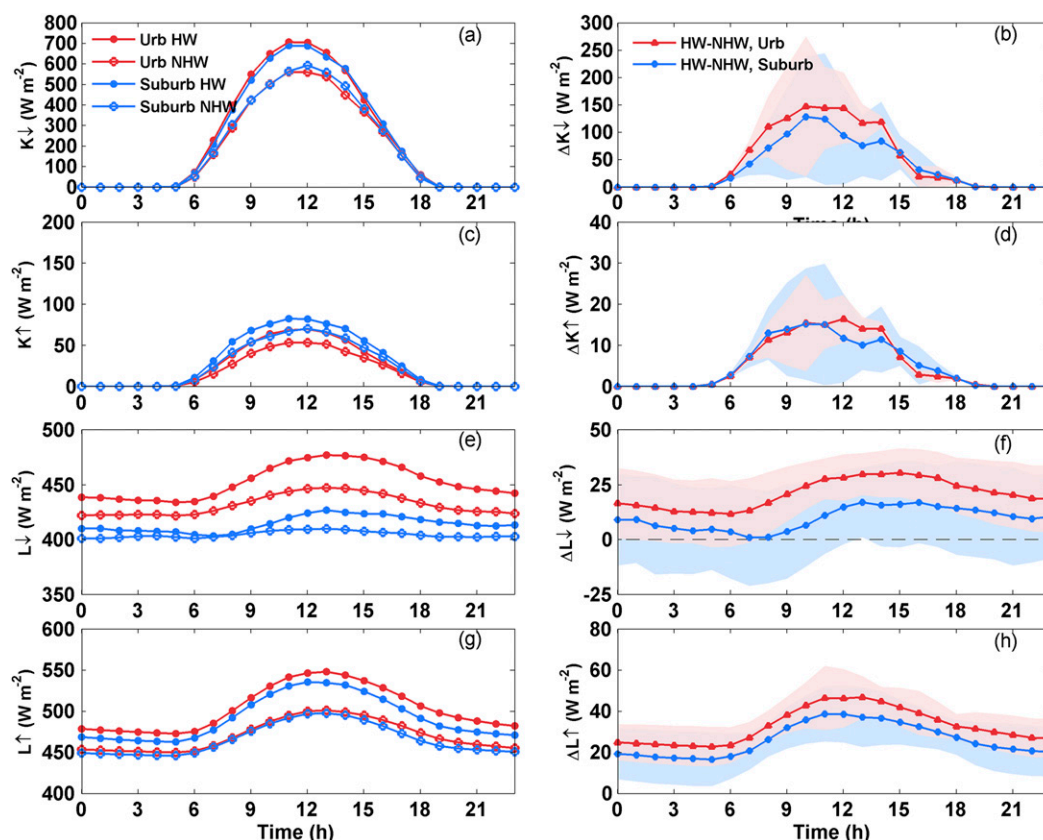
FIG. 5. Mean diurnal variations of the (a) downward shortwave radiation flux, (c) upward shortwave radiation flux, (e) downward longwave radiation flux, and (g) upward longwave radiation flux at the urban (XJH) and suburban (FX) sites. (b),(d),(f),(h) Their differences between HW and NHW conditions during 2016–18; the shaded areas denote the standard deviation.

are shown in Figs. 6a and 6b. The daytime Q^* at both urban and suburban sites increases under HW conditions. The biggest increase is about $128\,\mathrm{W\,m^{-2}}$ at the urban site and is about $115\,\mathrm{W\,m^{-2}}$ at the suburban site. The nighttime Q^* are more negative during HWs. The Q^* at the urban site is larger than its counterpart at the suburban site throughout the day, and this contrast becomes stronger under HW conditions (Fig. 6b). The increase of this positive urban–suburban Q^* difference under HW conditions results in more net radiation input in the urban area.

2) DIURNAL VARIATIONS OF SENSIBLE AND LATENT HEAT FLUXES

Figures 6c–f further show the mean diurnal variations of sensible heat flux Q_H and latent heat flux Q_E under HW and NHW conditions and the HW–NHW differences. Because of the limited vegetation cover and the large fraction of impervious surface, Q_H is consistently larger than Q_E at the urban site. On the other hand, the magnitude of Q_H and Q_E are close to each other with Q_E

slightly higher than Q_H at the suburban site. The urban Q_H are positive throughout the day, with nighttime values reaching $80–120\,\mathrm{W\,m^{-2}}$. The positive nighttime urban Q_H is possibly due to the heat storage released at night. The nighttime Q_H at the suburban site is near or slightly smaller than $0\,\mathrm{W\,m^{-2}}$. Q_H at the urban site is larger than that at the suburban site throughout the day. However, the daytime Q_E at the urban site is significantly smaller than that at suburban site, while the nighttime Q_E at these two sites are of similar magnitude, both slightly larger than 0. These characteristics lead to positive available energy (Q: the sum of sensible and latent heat fluxes) differences ($Q_u - Q_r$), especially at night, which will be further discussed later.

The HW-induced changes in the sensible heat flux and latent heat flux are different. The sensible heat flux Q_H at the urban site is larger under HW conditions than under NHW conditions all day, with the maximum difference reaching $140\,\mathrm{W\,m^{-2}}$ in the afternoon. The Q_H at the rural site also increases under HW conditions during daytime with the maximum increase around $100\,\mathrm{W\,m^{-2}}$,
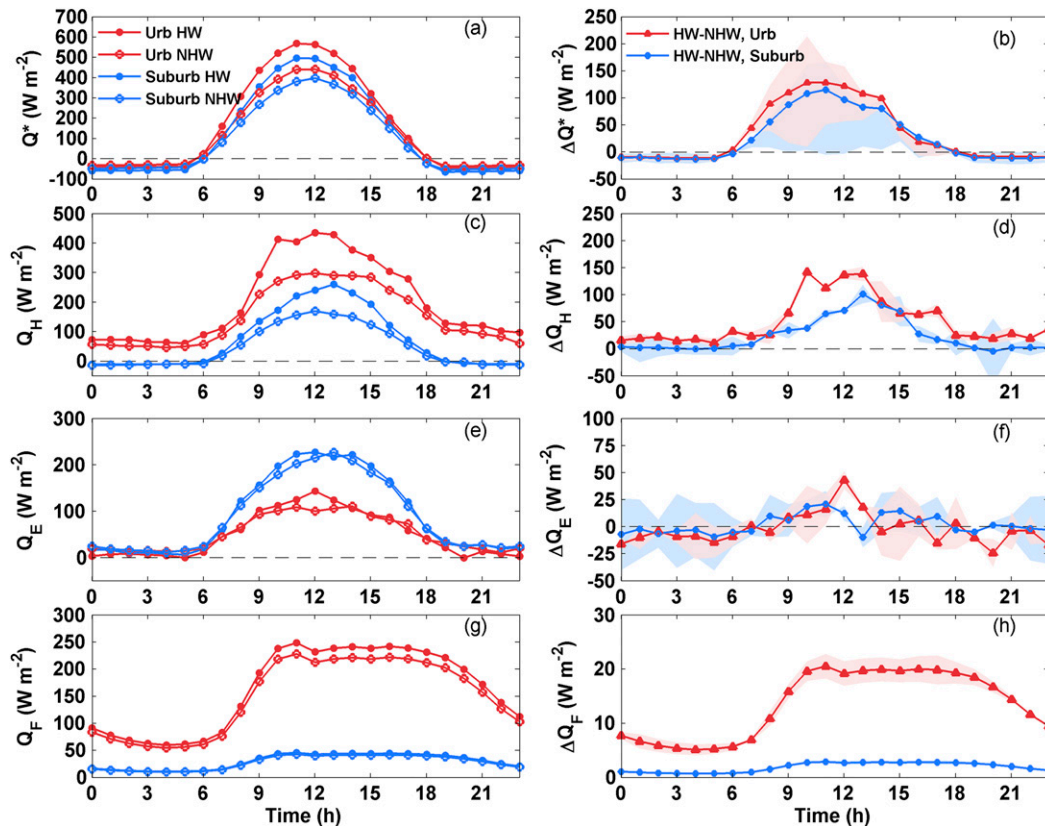
FIG. 6. As in Fig. 5, but for the (a) net all-wave radiation, (c) sensible heat, (e) latent heat, and (g) modeled anthropogenic heat fluxes.

but slightly decreases at night. This is different from the case in Beijing where Q_H at the rural site decreases throughout the day (Li et al. 2015). The increase of Q_H at the urban site is larger than that at the suburban site (Fig. 6c).

The HW-induced changes in the latent heat flux (Q_E) are smaller than those in Q_H, which is also different from the case in Beijing (Li et al. 2015). The diurnal variation of ΔQ_E at the urban site fluctuates with an overall decrease of $-2\,W\,m^{-2}$. The Q_E at the suburban site shows a slight increase ($2\,W\,m^{-2}$) during HW conditions. In summary, HWs cause larger amplifications of Q_H at both urban and suburban sites, while slight decreases of urban Q_E but increases of suburban Q_E. This contrasting response of the energy partitioning is mainly attributed to the different water availability for evaporation and vegetation coverage between the urban and suburban sites.

3) DIURNAL VARIATIONS OF THE ANTHROPOGENIC HEAT FLUX

Similar analysis is also conducted for the anthropogenic heat flux, as shown in Figs. 6g and 6h. The modeled anthropogenic heat flux Q_F at the urban site is very large

with the peak (1100 a.m.) around 250 and $230\,W\,m^{-2}$ under HW and NHW conditions, respectively (Fig. 5g). This is equivalent to about 48% of the net all-wave radiation (Fig. 6a), suggesting that Q_F plays an important role in the urban surface energy budget. The magnitude of Q_F at the urban site estimated in our study is much larger than that estimated by Sailor et al. (2015). This is because our study focuses on the neighborhood (site) scale while Sailor et al. (2015) focuses on the much larger city scale. Sailor et al. (2015) estimated the Q_F in Shanghai by extrapolating from that of U.S. cities using a correction factor based on the ratio of per capita energy consumption in the target country (China) to that in the United States. The larger population density around the urban site results in the much larger magnitude of Q_F. This is consistent with findings in other Asian city centers. For example, the winter daytime Q_F on average reached $400\,W\,m^{-2}$ in central Tokyo (Ichinose et al. 1999). The maximum annual mean Q_F averaged over a $1\,km \times 1\,km$ grid area was $27\,W\,m^{-2}$ in Seoul, 198 in Gyeonggi, and $320\,W\,m^{-2}$ in Incheon, South Korea (Lee et al. 2009). The diurnal peak Q_F was up to $550\,W\,m^{-2}$ in the central activities zone of London
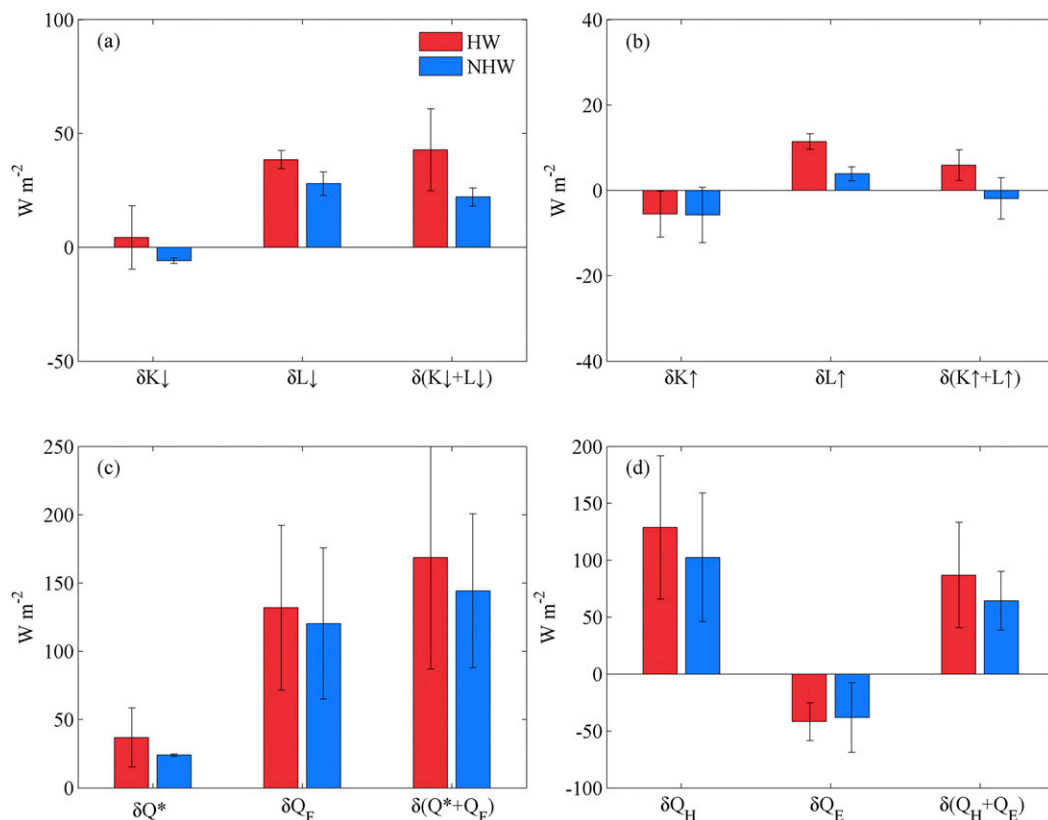
FIG. 7. The mean urban–suburban differences in (a) incoming shortwave radiation ($\delta K\downarrow$), incoming longwave radiation ($\delta L\downarrow$), and total incoming radiation [$\delta(K\downarrow + L\downarrow)$]; (b) outgoing shortwave radiation ($\delta K\uparrow$), outgoing longwave radiation ($\delta L\uparrow$), and total outgoing radiation [$\delta(K\uparrow + L\uparrow)$]; (c) net all-wave radiation (δQ^*), anthropogenic heat flux (δQ_F), and their sum [$\delta(Q^* + Q_F)$]; and (d) sensible heat (δQ_H), latent heat (δQ_E), and the available energy [$\delta(Q_H + Q_E)$] under HW and NHW conditions. The error bars denote the standard deviation.

(Iamarino et al. 2012). The enhanced anthropogenic heat flux under HW conditions is mainly attributed to the increased building cooling energy consumption. The nocturnal Q_F at the urban site can also reach relatively large values around 50–100 W m^{-2}, thus contributing significantly to the nighttime UHII. The magnitude of Q_F at the suburban site is much smaller with the mean diurnal peak around 45 W m^{-2} because of the much sparser population density. Q_F at the suburban site is also enhanced under HW conditions compared with NHW conditions but the enhancement is weaker than that at the urban site. As can be seen in Fig. 6h, the amplification of the daily maximum Q_F by HWs is about 20 and 3 W m^{-2} at the urban site and the suburban site, respectively.

4) THE MEAN URBAN–SUBURBAN DIFFERENCES OF THE SURFACE ENERGY BUDGETS

To summarize the different responses of urban and suburban surface energy budgets to HWs, the mean urban–suburban differences of the four components of

radiation, the net incoming and outgoing radiation, the net all-wave radiation, anthropogenic heat flux, sensible heat flux, latent heat flux and the available energy, are presented in Fig. 7. The mean urban–suburban difference of the downward shortwave radiation is very small under both HW and NHW conditions ($\delta K\downarrow < 10$ W m^{-2}), with this difference further narrowed under HW conditions. The urban–suburban difference of the downward longwave radiation ($\delta L\downarrow$) shows an obvious increase under HW conditions. The overall effect of $\delta K\downarrow$ and $\delta L\downarrow$ is the more downward radiation [$\delta(K\downarrow + L\downarrow)$] under HW conditions. The urban–suburban difference of the upward shortwave radiation ($\delta K\uparrow$) is negative and close to each other under HW and NHW conditions. The response of the $\delta L\uparrow$ is similar to $\delta L\downarrow$ with an obvious increase under HW conditions. Hence the total upward radiation difference [$\delta(K\uparrow + L\uparrow)$] increases during HW conditions. As a result, the increase of δQ^* is smaller than that of the total downward radiation difference [$\delta(K\downarrow + L\downarrow)$]. The urban–suburban contrast of the anthropogenic heat flux (δQ_F) is clearly increased under HW conditions.
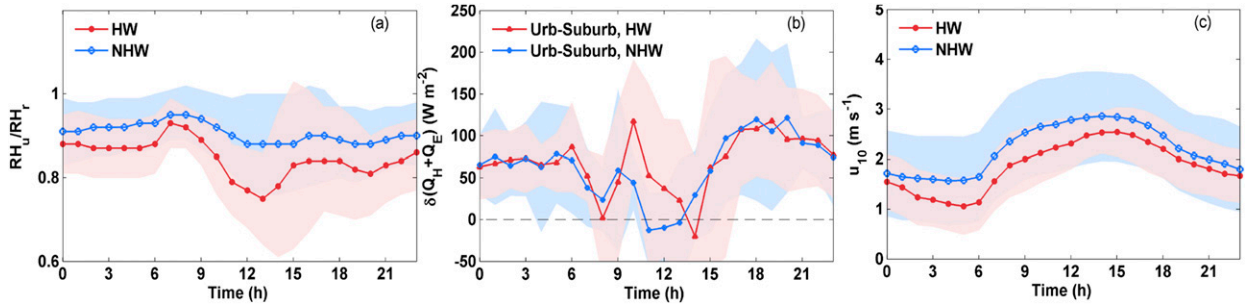
FIG. 8. Mean diurnal variations of (a) the relative humidity ratio RH_u/RH_r between urban and suburban sites, (b) the urban–suburban difference of available energy $Q_u - Q_r$, and (c) the regional wind speed at 10 m under HW and NHW conditions.

This increase, combined with the increase of δQ^*, leads to a stronger forcing $[\delta(Q^* + Q_F)]$ to the urban surface energy budget relative to its rural counterpart.

The stronger forcing received by the urban surface under HW conditions leads to the stronger increase of urban sensible heat flux relative to the rural sensible heat flux (i.e., δQ_H is enhanced), while the negative urban–suburban latent heat flux difference ($\delta Q_E < 0$) slightly increases (i.e., δQ_E becomes slightly more negative) under HW conditions. This shows the contrasting responses of energy partitioning to HWs at the urban and suburban sites. The combined effect is that the urban–suburban difference of the available energy $[\delta(Q_H + Q_E)]$ is amplified under HW relative to NHW conditions.

Section 3b has demonstrated that the land breeze–sea breeze plays an important role in controlling the synergistic interactions between HWs and UHIs. Therefore, it is important to examine whether the responses of surface energy budgets are similar under land-breeze and sea-breeze conditions. However, because of the data limitation for land-breeze/HW cases, we could only analyze the responses of the urban and suburban surface energy budgets to HWs under sea-breeze conditions. We find that the energy budget differences under only sea-breeze conditions are qualitatively similar to those shown in Figs. 5–7 (not shown), suggesting that the observed responses of surface energy budget to HWs are robust.

d. Interpretation of UHI–HW synergies based on the analytical model

1) MOISTURE AVAILABILITY

According to the analytical model (see appendix), the ratio between urban and suburban surface moisture availability β_u/β_r is a major controlling factor of UHII. Because there is no soil moisture measurement at the study sites, the air relative humidity (RH) is used instead since its definition is the same as β only the measurement height is at 2 m rather than at the surface. From

Table 2, one can see that RH at the urban site is consistently lower than the suburban sites and the coastal FX site has the largest RH values. Figure 8a shows the mean diurnal patterns of RH_u/RH_r during HW and NHW conditions. RH_u/RH_r is smaller than 1 under both HW and NHW conditions, indicating that the urban surface is always drier than its suburban counterpart. We also examine the ratio of water vapor pressure, which shows similar patterns (not shown). This is mainly caused by the larger impervious surface fraction and the limited vegetation cover at the urban site. The diurnal variation of RH_u/RH_r during NHW periods is relatively stable ranging between 0.88 and 0.95. Relative to the RH_u/RH_r under NHW periods, the RH_u/RH_r during HW periods is smaller throughout the day and has a larger diurnal variation (0.75–0.93). This indicates that the urban surface becomes even drier than the suburban surface during HWs, which further suppresses evaporation and enhances the UHII. This is consistent with the results in Fig. 6.

2) REGIONAL WIND SPEED AND URBAN– SUBURBAN AVAILABLE ENERGY DIFFERENCE

Another major controlling factor on UHII from the analytical model is the combined effect of regional wind speed and the urban–rural available energy difference $[\delta(Q_u - Q_r)]$. From Fig. 7b we can see that the $\delta(Q_u - Q_r)$ is always positive under both HW and NHW conditions. Close inspection reveals that $\delta(Q_u - Q_r)$ is positive all day except a few hours around 1300 LST when the values of $\delta(Q_u - Q_r)$ are slightly negative (Fig. 6b). However, there is little difference between HW and NHW conditions in terms of the diurnal variation of $\delta(Q_u - Q_r)$ (Fig. 8b). Hence, to understand how the UHII is enhanced under HWs requires us to examine how the regional wind speed changes.

Table 2 shows that the mean wind speed at the urban site is much weaker ($<1\,\mathrm{m\,s^{-1}}$) than the suburban sites because of the blocking effect of tall buildings, and the coastal site has the strongest wind speed. However,

given that the roughness length does not change with HWs, the wind speed difference between urban and rural areas is not considered here. Instead, the regional wind speed at 10 m u_{10} measured by the 11 weather stations in Shanghai is examined. From Fig. 8c it is clear that the regional wind speed becomes consistently smaller during HW periods relative to NHW counterparts, which is consistent with the results shown in Table 2. The biggest decrease of u_{10} is about $0.5 \, \text{m s}^{-1}$ at 1000 LST. On the basis of the analytical model, it is seen that the decrease of u_{10}, combined with the positive $\delta(Q_u - Q_r)$, enhances the UHII under HWs.

4. Conclusions and discussion

In this study, the synergistic interactions between UHIs and HWs are studied using a comprehensive dataset collected over the city of Shanghai. The underlying physical mechanisms are elucidated by investigating the contrasting responses of urban–suburban surface energy budgets and moisture availability to HWs, as well as the response of regional wind field to HWs. In comparison with previous studies that did not quantify the anthropogenic heat flux Q_F, we estimate Q_F using a top-down model and quantify how Q_F changes under HWs. The influence of land-breeze–sea-breeze circulation on the UHII and its association with HWs are also examined.

The results show that the UHII is consistently enhanced under HW conditions for both coastal and inland reference sites under all meteorological conditions. The diurnal patterns of UHII are quite different with stronger daytime UHII for the coastal site while stronger nighttime UHII for the inland site. We further classify the study period into optimal days for identifying UHI (light wind, cloudless, low humidity, and no precipitation) and nonoptimal days. The synergistic effects between HWs and UHIs are clear at the coastal site. For the inland site, the synergistic interactions remain strong under nonoptimal days but only exist during daytime under optimal days.

The contrasting responses of urban and suburban surface energy budgets to HWs are examined. The urban–suburban differences of incoming and outgoing shortwave radiation under HWs are similar to those under NHWs. On the other hand, the urban site receives more incoming radiation and produces more outgoing longwave radiation under HWs relative to the suburban site. The combined effect is that the urban–suburban difference of the net all-wave radiation Q^* is larger under HW conditions than NHW conditions. The urban–suburban contrast of the anthropogenic heat flux increases under HW conditions primarily because of additional energy consumption for air conditioning in urban areas. All of

these translate into a larger forcing for the urban surface energy budget under HWs.

Because of the limited vegetation cover and soil water availability at the urban site, the urban sensible heat flux increases all day under HW conditions with the maximum increase in the afternoon. The suburban increase of Q_H is smaller than the urban counterpart, with a slight decrease at night. The latent heat flux Q_E at the urban site shows a small decreasing trend under HW conditions, while a small increase of Q_E is observed at the suburban site. This change of energy partitioning is favorable for a stronger UHII.

An analytical model is further utilized to interpret the results. Specifically, we investigate the two major controlling factors identified by the model, that is, the ratio of urban and suburban surface moisture availability (approximated by the 2-m relative humidity) RH_u/RH_r, and the combined effect of regional wind speed and the urban–suburban available energy difference. It is found that the RH_u/RH_r is smaller under HW conditions than under NHW conditions throughout the day, which indicates that the urban surface becomes even drier during HWs than the suburban surfaces, suppressing evapotranspiration and enhancing the UHII. The regional wind speed is weakened under HW conditions, which causes an increase in the UHII when combined with the positive urban–suburban available energy difference.

Our analysis reveals multiple physical mechanisms contributing to the synergistic interactions between HWs and UHIs. While many of these mechanisms are expected to hold true for other regions (e.g., the stronger increase of urban net radiation and urban anthropogenic heat flux under HWs compared to their suburban counterparts), some mechanisms might depend on the specific urban–suburban settings. For example, while our study and Li et al. (2015) found a stronger increase of urban sensible heat flux and a smaller increase (or even a decrease) of urban latent heat flux under HWs relative to the suburban/rural counterparts, it can be expected that cities located in a desert climate might show the opposite response because of irrigation in cities (i.e., cities have more water availability for evapotranspiration than the surrounding areas). In addition, the regional wind speed is shown to play an important role, but whether the decreased regional wind speed under HWs as observed here is universal remains to be studied. For coastal cities, especially when the UHI is calculated using data from sites that can be influenced by land–sea breeze, whether the UHI is stronger under land breeze or sea breeze and whether land breeze or sea breeze will be favored by HWs are likely to be dependent on the specific locations of the urban and reference sites relative to the coastal line, the local geography, and the synoptic

conditions. The fact that many mechanisms contributing to the synergies between HWs and UHIs vary across cities may explain why synergies between HWs and UHIs are only observed in certain metropolitan regions and/or for certain HW events. However, our analysis emphasizes the importance to study the physical mechanisms for the synergies between HWs and UHIs, in addition to identifying statistical associations between the two phenomena.

The findings of this study provide some insights into urban heat mitigation and future urban planning. For example, increases of urban green infrastructure, urban irrigation, and water fountains are encouraged to enhance the urban water availability (Li et al. 2014; Tewari et al. 2019). The construction of urban ventilation corridors is also an effective strategy for heat mitigation as the enhanced regional wind speed can significantly improve the cooling effect. Because the urban–suburban anthropogenic heat flux difference is identified as a critical contributor to the synergies between HWs and UHIs, it is also important to improve building energy efficiencies in highly populated urban areas. However, it should be also stressed that the effects of these urban heat mitigation strategies might be geographically dependent (Georgescu et al. 2014), thus a careful design of appropriate strategies is needed for each city. In addition, how the implementation of these urban heat mitigation strategies, together with the continuous urban expansion and future climate change, would shape the local urban climate, remains an important research topic to be explored in future work.

APPENDIX

An Analytical Model for UHII

This study employs the analytical model developed by Li and Bou-Zeid (2013) in which UHII is given as

$$
\begin{aligned}
\text{UHII} = T_u(x, z) - T_r(z) = (1 - \beta_u/\beta_r)T^*_{rs}f_1(x, z) \\
+ g(u_{10})(Q_u - Q_r)f_2(x, z),
\end{aligned}
\tag{A1}
$$

where $T_u(x, z)$ and $T_r(z)$ are the air temperature over urban and rural areas, respectively, and x and z are the streamwise and vertical coordinates, respectively. For the range $0 < x < x_u$, the surface represents urban, where x_u indicates the size of the urban patch. When $x > x_u$ or $x < 0$, the surface becomes rural. Height $z = 0$ represents the surface. Because the rural surface is assumed to be infinitely long, $T_r(z)$ is only a function of z, which indicates that the incoming flow is in equilibrium with the upwind rural surface conditions. Variables β_u and β_r denote the urban and rural surface moisture availability, respectively, and are the ratio of the actual specific humidity to the saturated specific humidity. The value of β ranges from 0 to 1; the larger the value is, the wetter is the surface. Hence, β_u/β_r represents the contrast between urban and rural surface wetness, which is primarily determined by the contrast of urban–rural soil moisture content. $T^*_{rs} = q_{rs}/(c_p/L_v + \alpha\beta_u)$ is a characteristic temperature scale denoting the sensitivity of UHII to urban–rural surface moisture availability difference, where q_{rs} (kg kg^{-1}) is the actual rural surface specific humidity, c_p (J kg^{-1} K^{-1}) is the atmospheric specific heat capacity at constant pressure, L_v (J kg^{-1}) is the latent heat of water vaporization, and α is approximately a constant ($=1.87 \times 10^{-3}$ K^{-1}). The $g(u_{10})$ is a positive function that decreases with increasing regional wind speed u_{10}. Difference $Q_u - Q_r$ is the available energy (which is the sum of sensible and latent heat fluxes) difference between urban and rural surfaces; $f_1(x, z)$ and $f_2(x, z)$ are functions of positions only x and z, which are generated by solving the advection–diffusion equations, and both are positive.

From Eq. (A1), it can be seen that there are two major factors that impact the UHII. The first [the first term of the rhs of Eq. (A1)] is the ratio between urban and rural surface moisture availability (β_u/β_r), and the second [the second term of the rhs of Eq. (A1)] is a combination of regional wind speed effect (u_{10}) and the urban–rural difference of available energy ($Q_u - Q_r$). The sign of $Q_u - Q_r$ determines whether the second term has a positive or negative effect on the UHII (Li et al. 2016). During HWs, the urban and rural surface moisture condition, available energy, and wind speed will all show different characteristics than during non-HW conditions. Therefore, this analytical model can be an effective tool to elucidate the physical mechanisms that are responsible for the synergistic interactions between UHIs and HWs.

REFERENCES

Allen, L., F. Lindberg, and C. S. B. Grimmond, 2011: Global to city scale urban anthropogenic heat flux: Model and variability. *Int. J. Climatol.*, **31**, 1990–2005, https://doi.org/10.1002/joc.2210.

Anderson, B. G., and M. L. Bell, 2009: Weather-related mortality: How heat, cold, and heat waves affect mortality in the United States. *Epidemiology*, **20**, 205–213, https://doi.org/10.1097/EDE.0b013e318190ee08.

——, and ——, 2011: Heat waves in the United States: Mortality risk during heat waves and effect modification by heat wave characteristics in 43 U.S. communities. *Environ. Health Perspect.*, **119**, 210–218, https://doi.org/10.1289/ehp.1002313.

Ao, X., and Coauthors, 2016a: Heat, water and carbon exchanges in the tall megacity of Shanghai: Challenges and results. *Int. J. Climatol.*, **36**, 4608–4624, https://doi.org/10.1002/joc.4657.

——, C. S. B. Grimmond, D. Liu, Z. Han, P. Hu, Y. Wang, X. Zhen, and J. Tan, 2016b: Radiation fluxes in a business district of Shanghai, China. *J. Appl. Meteor. Climatol.*, **55**, 2451–2468, https://doi.org/10.1175/JAMC-D-16-0082.1.

——, and Coauthors, 2018: Evaluation of the Surface Urban Energy and Water balance Scheme (SUEWS) at a dense urban site in Shanghai: Sensitivity to anthropogenic heat and irrigation. *J. Hydrometeor.*, **19**, 1983–2005, https://doi.org/10.1175/JHM-D-18-0057.1.

Arnfield, A. J., 2003: Two decades of urban climate research: A review of turbulence, exchanges of energy and water, and the urban heat island. *Int. J. Climatol.*, **23**, 1–26, https://doi.org/10.1002/joc.859.

Basara, J. B., H. G. Basara, B. G. Illston, and K. C. Crawford, 2010: The impact of the urban heat island during an intense heat wave in Oklahoma City. *Adv. Meteor.*, **2010**, 185–194, https://doi.org/10.1155/2010/230365.

Cao, M., P. Rosado, Z. Lin, R. Levinson, and D. Millstein, 2015: Cool roofs in Guangzhou, China: Outdoor air temperature reductions during heat waves and typical summer conditions. *Environ. Sci. Technol.*, **49**, 14 672, https://doi.org/10.1021/acs.est.5b04886.

Chen, F., S. Miao, M. Tewari, J. W. Bao, and H. Kusaka, 2011: A numerical study of interactions between surface forcing and sea breeze circulations and their effects on stagnation in the greater Houston area. *J. Geophys. Res.*, **116**, D12105, https://doi.org/10.1029/2010JD015533.

Chow, W. T., F. Salamanca, M. Georgescu, A. Mahalov, J. M. Milne, and B. L. Ruddell, 2014: A multi-method and multi-scale approach for estimating city-wide anthropogenic heat fluxes. *Atmos. Environ.*, **99**, 64–76, https://doi.org/10.1016/j.atmosenv.2014.09.053.

Christen, A., and Coauthors, 2011: Validation of modeled carbon-dioxide emissions from an urban neighborhood with direct eddy-covariance measurements. *Atmos. Environ.*, **45**, 6057–6069, https://doi.org/10.1016/j.atmosenv.2011.07.040.

Cui, L., and J. Shi, 2012: Urbanization and its environmental effects in Shanghai, China. *Urban Climate*, **2**, 1–15, https://doi.org/10.1016/j.uclim.2012.10.008.

Depietri, Y., F. G. Renaud, and G. Kallis, 2012: Heat waves and floods in urban areas: a policy-oriented review of ecosystem services. *Sustainability Sci.*, **7**, 95–107, https://doi.org/10.1007/s11625-011-0142-4.

Eastin, M. D., M. Baber, A. Boucher, S. Dibari, R. Hubler, B. Stimac-Spalding, and T. Winesett, 2018: Temporal variability of the Charlotte (sub)-urban heat island. *J. Appl. Meteor. Climatol.*, **57**, 81–102, https://doi.org/10.1175/JAMC-D-17-0099.1.

Enomoto, T., 2004: Interannual variability of the Bonin high associated with the propagation of Rossby waves along the Asian jet. *J. Meteor. Soc. Japan*, **82**, 1019–1034, https://doi.org/10.2151/jmsj.2004.1019.

Foken, T., 2008: The energy balance closure problem: An overview. *Ecol. Appl.*, **18**, 1351–1367, https://doi.org/10.1890/06-0922.1.

Founda, D., and M. Santamouris, 2017: Synergies between urban heat island and heat waves in Athens (Greece), during an extremely hot summer (2012). *Sci. Rep.*, **7**, 10973, https://doi.org/10.1038/s41598-017-11407-6.

——, F. Pierros, M. Petrakis, and C. Zerefos, 2015: Inter-decadal variations and trends of the urban heat island in Athens (Greece) and its response to heat waves. *Atmos. Res.*, **161–162**, 1–13, https://doi.org/10.1016/j.atmosres.2015.03.016.

Gabey, A., C. S. B. Grimmond, and I. Capel-Timms, 2018: Anthropogenic heat flux: Advisable spatial resolutions when input data are scarce. *Theor. Appl. Climatol.*, https://doi.org/10.1007/s00704-018-2367-y.

Gabriel, K. M., and W. R. Endlicher, 2011: Urban and rural mortality rates during heat waves in Berlin and Brandenburg, Germany. *Environ. Pollut.*, **159**, 2044–2050, https://doi.org/10.1016/j.envpol.2011.01.016.

Geddes, J. A., J. G. Murphy, J. Schurman, A. Petroff, and S. C. Thomas, 2014: Net ecosystem exchange of an uneven-aged managed forest in central Ontario, and the impact of a spring heat wave event. *Agric. For. Meteor.*, **198–199**, 105–115, https://doi.org/10.1016/j.agrformet.2014.08.008.

Georgescu, M., P. E. Morefield, B. G. Bierwagen, and C. P. Weaver, 2014: Urban adaptation can roll back warming of emerging megapolitan regions. *Proc. Natl. Acad. Sci. USA*, **111**, 2909–2914, https://doi.org/10.1073/pnas.1322280111.

Grimmond, C. S. B., 2007: Urbanization and global environmental change: Local effects of urban warming. *Geogr. J.*, **173**, 83–88, https://doi.org/10.1111/j.1475-4959.2007.232_3.x.

Grumm, R. H., 2011: The central European and Russian heat event of July–August 2010. *Bull. Amer. Meteor. Soc.*, **92**, 1285–1296, https://doi.org/10.1175/2011BAMS3174.1.

Haeger-Eugensson, M., and B. Holmer, 1999: Advection caused by the urban heat island circulation as a regulating factor on the nocturnal urban heat island. *Int. J. Climatol.*, **19**, 975–988, https://doi.org/10.1002/(SICI)1097-0088(199907)19:9<975::AID-JOC399>3.0.CO;2-J.

He, C., T. Zhou, A. Lin, B. Wu, D. Gu, C. Li, and B. Zheng, 2015: Enhanced or weakened western North Pacific subtropical high under global warming? *Sci. Rep.*, **5**, 16 771, https://doi.org/10.1038/srep16771.

Hidalgo, J., V. Masson, and L. Gimeno, 2010: Scaling the daytime urban heat island and urban-breeze circulation. *J. Appl. Meteor. Climatol.*, **49**, 889–901, https://doi.org/10.1175/2009JAMC2195.1.

Hoffert, M. I., and Coauthors, 2002: Advanced technology paths to global climate stability: Energy for a greenhouse planet. *Science*, **298**, 981–987, https://doi.org/10.1126/science.1072357.

Hu, K., and Coauthors, 2019: Evidence for urban–rural disparity in temperature–mortality relationships in Zhejiang Province, China. *Environ. Health Perspect.*, **127**, 037001, https://doi.org/10.1289/EHP3556.

Iamarino, M., S. Beevers, and C. S. B. Grimmond, 2012: High-resolution (space, time) anthropogenic heat emissions: London 1970–2025. *Int. J. Climatol.*, **32**, 1754–1767, https://doi.org/10.1002/joc.2390.

Ichinose, T., K. Shimodozono, and K. Hanaki, 1999: Impact of anthropogenic heat on urban climate in Tokyo. *Atmos. Environ.*, **33**, 3897–3909, https://doi.org/10.1016/S1352-2310(99)00132-6.

Kalkstein, L. S., J. S. Greene, D. M. Mills, A. D. Perrin, J. P. Samenow, and C. Jean-Claude, 2008: Analog European heat waves for U.S. cities to analyze impacts on heat-related mortality. *Bull. Amer. Meteor. Soc.*, **89**, 75–85, https://doi.org/10.1175/BAMS-89-1-75.

Kalnay, E., and M. Cai, 2003: Impact of urbanization and land-use change on climate. *Nature*, **423**, 528–531, https://doi.org/10.1038/nature01675.

Kim, H. W., and D. K. Lee, 2006: An observational study of mesoscale convective systems with heavy rainfall over the Korean Peninsula. *Wea. Forecasting*, **21**, 125–148, https://doi.org/10.1175/WAF912.1.

Knutson, T. R., F. R. Zeng, and A. T. Wittenberg, 2013: The extreme March–May 2012 warm anomaly over the eastern United States: Global context and multi-model trend analysis [in "Explaining Extreme Events of 2012 from a Climate Perspective"]. *Bull. Amer. Meteor. Soc.*, **94** (9), S13–S17, https://doi.org/10.1175/BAMS-D-13-00085.1.

Kormann, R., and F. X. Meixner, 2001: An analytical footprint model for non-neutral stratification. *Bound.-Layer Meteor.*, **99**, 207–224, https://doi.org/10.1023/A:1018991015119.

Lau, N. C., and M. J. Nath, 2012: A model study of heat waves over North America: Meteorological aspects and projections for the 21st century. *J. Climate*, **25**, 4761–4784, https://doi.org/10.1175/JCLI-D-11-00575.1.

——, and J. J. Ploshay, 2013: Model projections of the changes in atmospheric circulation and surface climate over North America, North Atlantic and Europe in the 21st century. *J. Climate*, **26**, 9603–9620, https://doi.org/10.1175/JCLI-D-13-00151.1.

Lee, S. H., C. K. Song, J. J. Baik, and S. U. Park, 2009: Estimation of anthropogenic heat emission in the Gyeong-In region of Korea. *Theor. Appl. Climatol.*, **96**, 291–303, https://doi.org/10.1007/s00704-008-0040-6.

Li, D., and E. Bou-Zeid, 2013: Synergistic interactions between urban heat islands and heat waves: The impact in cities is larger than the sum of its parts. *J. Appl. Meteor. Climatol.*, **52**, 2051–2064, https://doi.org/10.1175/JAMC-D-13-02.1.

——, ——, and M. Oppenheimer, 2014: The effectiveness of cool and green roofs as urban heat island mitigation strategies. *Environ. Res. Lett.*, **9**, 055002, https://doi.org/10.1088/1748-9326/9/5/055002.

——, T. Sun, M. Liu, L. Yang, L. Wang, and Z. Gao, 2015: Contrasting responses of urban and rural surface energy budgets to heat waves explain synergies between urban heat islands and heat waves. *Environ. Res. Lett.*, **10**, 054009, https://doi.org/10.1088/1748-9326/10/5/054009.

——, ——, ——, L. Wang, and Z. Gao, 2016: Changes in wind speed under heat waves enhance urban heat Islands in the Beijing metropolitan area. *J. Appl. Meteor. Climatol.*, **55**, 2369–2375, https://doi.org/10.1175/JAMC-D-16-0102.1.

Li, W., L. Li, M. Ting, and Y. Liu, 2012: Intensification of Northern Hemisphere subtropical highs in a warming climate. *Nat. Geosci.*, **5**, 830–834, https://doi.org/10.1038/ngeo1590.

Lindberg, F., C. S. B. Grimmond, N. Yogeswaran, K. Kotthaus, and L. Allen, 2013: Impact of city changes and weather on anthropogenic heat flux in Europe 1995–2015. *Urban Climate*, **4**, 1–15, https://doi.org/10.1016/j.uclim.2013.03.002.

Liu, D., and Coauthors, 2018: A new model to downscale urban and rural surface and air temperatures evaluated in Shanghai, China. *J. Appl. Meteor. Climatol.*, **57**, 2267–2283, https://doi.org/10.1175/JAMC-D-17-0255.1.

Liu, H., and L. Cao, 2013: The relationship between power load and meteorological factors with refined power load forecast in Shanghai (in Chinese). *J. Appl. Meteor. Sci.*, **24**, 455–463.

Liu, Y., X. Fang, Y. Xu, S. Zhang, and Q. Luan, 2018: Assessment of surface urban heat island across China's three main urban agglomerations. *Theor. Appl. Climatol.*, **133**, 4734–88, https://doi.org/10.1007/s00704-017-2197-3.

Loikith, P. C., and A. J. Broccoli, 2012: Characteristics of observed atmospheric circulation patterns associated with temperature extremes over North America. *J. Climate*, **25**, 7266–7281, https://doi.org/10.1175/JCLI-D-11-00709.1.

Ma, S., T. Zhou, D. Stone, O. Angélil, and H. Shiogama, 2017: Attribution of the July–August 2013 heat event in Central and Eastern China to anthropogenic greenhouse gas emissions. *Environ. Res. Lett.*, **12**, 054020, https://doi.org/10.1088/1748-9326/aa69d2.

Matsumura, S., S. Sugimoto, and T. Sato, 2015: Recent intensification of the western Pacific subtropical high associated with the East Asian summer monsoon. *J. Climate*, **28**, 2873–2883, https://doi.org/10.1175/JCLI-D-14-00569.1.

Meehl, G. A., and C. Tebaldi, 2004: More intense, more frequent, and longer lasting heat waves in the 21st century. *Science*, **305**, 994–997, https://doi.org/10.1126/science.1098704.

Meir, T., P. M. Orton, J. Pullen, T. Holt, W. T. Thompson, and M. F. Arend, 2013: Forecasting the New York City urban heat island and sea breeze during extreme heat events. *Wea. Forecasting*, **28**, 1460–1477, https://doi.org/10.1175/WAF-D-13-00012.1.

Miao, S., F. Chen, M. A. Lemone, M. Tewari, Q. Li, and Y. Wang, 2009: An observational and modeling study of characteristics of urban heat island and boundary layer structures in Beijing. *J. Appl. Meteor. Climatol.*, **48**, 484–501, https://doi.org/10.1175/2008JAMC1909.1.

Miller, N. L., K. Hayhoe, J. Jin, and M. Auffhammer, 2008: Climate, extreme heat, and electricity demand in California. *J. Appl. Meteor. Climatol.*, **47**, 1834–1844, https://doi.org/10.1175/2007JAMC1480.1.

Mora, C., and Coauthors, 2017: Global risk of deadly heat. *Nat. Climate Change*, **7**, 501–506, https://doi.org/10.1038/nclimate3322.

Oke, T. R., 1982: The energetic basis of the urban heat-island. *Quart. J. Roy. Meteor. Soc.*, **108**, 1–24, https://doi.org/10.1002/qj.49710845502.

Peterson, T. C., and Coauthors, 2013: Monitoring and understanding changes in heat waves, cold waves, floods and droughts in the United States: State of knowledge. *Bull. Amer. Meteor. Soc.*, **94**, 821–834, https://doi.org/10.1175/BAMS-D-12-00066.1.

Ramamurthy, P., and E. Bou-Zeid, 2017: Heatwaves and urban heat islands: A comparative analysis of multiple cities. *J. Geophys. Res. Atmos.*, **122**, 168–178, https://doi.org/10.1002/2016JD025357.

——, D. Li, and E. Bou-Zeid, 2017: High-resolution simulation of heatwave events in New York City. *Theor. Appl. Climatol.*, **128**, 89–102, https://doi.org/10.1007/s00704-015-1703-8.

Robinson, P. J., 2001: On the definition of a heat wave. *J. Appl. Meteor.*, **40**, 762–775, https://doi.org/10.1175/1520-0450(2001)040<0762:OTDOAH>2.0.CO;2.

Roth, M., 2000: Review of atmospheric turbulence over cities. *Quart. J. Roy. Meteor. Soc.*, **126**, 941–990, https://doi.org/10.1002/qj.49712656409.

Russo, S., and Coauthors, 2015: Magnitude of extreme heat waves in present climate and their projection in a warming world. *J. Geophys. Res. Atmos.*, **119**, 12 500–12 512, https://doi.org/10.1002/2014JD022098.

Sailor, D. J., 2011: A review of methods for estimating anthropogenic heat and moisture emissions in the urban environment. *Int. J. Climatol.*, **31**, 189–199, https://doi.org/10.1002/joc.2106.

——, and L. Lu, 2004: A top-down methodology for developing diurnal and seasonal anthropogenic heating profiles for urban areas. *Atmos. Environ.*, **38**, 2737–2748, https://doi.org/10.1016/j.atmosenv.2004.01.034.

——, M. Georgescu, J. M. Milne, and M. A. Hart, 2015: Development of a national anthropogenic heating database with an extrapolation for international cities. *Atmos. Environ.*, **118**, 7–18, https://doi.org/10.1016/j.atmosenv.2015.07.016.

Schatz, J., and C. J. Kucharik, 2015: Urban climate effects on extreme temperatures in Madison, Wisconsin, USA. *Environ. Res. Lett.*, **10**, 094024, https://doi.org/10.1088/1748-9326/10/9/094024.

Scott, A. A., D. W. Waugh, and B. F. Zaitchik, 2018: Reduced urban heat island intensity under warmer conditions. *Environ. Res. Lett.*, **13**, 064003, https://doi.org/10.1088/1748-9326/aabd6c.

Sun, T., S. Kotthaus, D. Li, H. C. Ward, Z. Gao, G. Ni, and C. S. B. Grimmond, 2017: Attribution and mitigation of heat wave-induced urban heat storage change. *Environ. Res. Lett.*, **12**, 114007, https://doi.org/10.1088/1748-9326/aa922a.

Tan, J. G., and Coauthors, 2010: The urban heat island and its impact on heat waves and human health in Shanghai. *Int. J. Biometeor.*, **54**, 75–84, https://doi.org/10.1007/s00484-009-0256-x.

Tewari, M., J. Yang, H. Kusaka, F. Salamanca, W. Campbell, and L. Treinish, 2019: Interaction of urban heat islands and heat waves under current and future climate conditions and their mitigation using green and cool roofs in New York City and Phoenix, Arizona. *Environ. Res. Lett.*, **14**, 034002, https://doi.org/10.1088/1748-9326/aaf431.

Wreford, A., and W. Neiladger, 2010: Adaptation in agriculture: Historic effects of heat waves and droughts on UK agriculture. *Int. J. Agric. Sustainability*, **8**, 278–289, https://doi.org/10.3763/ijas.2010.0482.

Xia, J., K. Tu, Z. Yan, and Y. Qi, 2016: The super-heat wave in eastern China during July–August 2013: A perspective of climate change. *Int. J. Climatol.*, **36**, 1291–1298, https://doi.org/10.1002/joc.4424.

Yu, J., and J. Wen, 2016: Multi-criteria satisfaction assessment of the spatial distribution of urban emergency shelters based on high-precision population estimation. *Int. J. Disaster Risk Sci.*, **7**, 413–429, https://doi.org/10.1007/s13753-016-0111-8.

Zaitchik, B. F., A. K. Macalady, L. R. Bonneau, and R. B. Smith, 2006: Europe's 2003 heat wave: A satellite view of impacts and land–atmosphere feedbacks. *Int. J. Climatol.*, **26**, 743–769, https://doi.org/10.1002/joc.1280.

Zhao, L., X. Lee, R. B. Smith, and K. Oleson, 2014: Strong contributions of local background climate to urban heat islands. *Nature*, **511**, 216–219, https://doi.org/10.1038/nature13462.

——, M. Oppenheimer, Q. Zhu, J. W. Baldwin, K. L. Ebi, E. Bou-Zeid, K. Guan, and X. Liu, 2018: Interactions between urban heat islands and heat waves. *Environ. Res. Lett.*, **13**, 034003, https://doi.org/10.1088/1748-9326/aa9f73.

Zhong, W., D. Wang, D. Xie, and L. Yan, 2017: Dynamic characteristics of Shanghai's population distribution using cell phone signaling data (in Chinese). *Geogr. Res.*, **36**, 972–984, https://doi.org/10.11821/dlyj201705013.

Zhou, D., S. Zhao, L. Zhang, G. Sun, and Y. Liu, 2015: The footprint of urban heat island effect in china. *Sci. Rep.*, **5**, 11160, https://doi.org/10.1038/srep11160.

Zhou, L., R. E. Dickinson, Y. Tian, J. Fang, Q. Li, R. K. Kaufmann, C. J. Tucker, and R. B. Myneni, 2004: Evidence for a significant urbanization effect on climate in China. *Proc. Natl. Acad. Sci. USA*, **101**, 9540–9544, https://doi.org/10.1073/pnas.0400357101.

Zhou, Y., and J. M. Shepherd, 2010: Atlanta's urban heat island under extreme heat conditions and potential mitigation strategies. *Nat. Hazards*, **52**, 639–668, https://doi.org/10.1007/s11069-009-9406-z.